journal homepage: www.brodogradnja.fsb.hr

Brodogradnja

An International Journal of Naval Architecture and Ocean Engineering for Research and Development

# Automatic Optimal Design Method for Minimum Total Resistance Hull Based on Enhanced FFD Method

*Shuhui Guo*[1], *Baoji Zhang*[*1], *Zheng Tian*[1], *Jie Liu*[2], *Hailin Tang*[1]

[1] *College of Ocean Science and Engineering, Shanghai Maritime University, Shanghai, 201306, China*
[2] *Merchant Marine College, Shanghai Maritime University, Shanghai, 201306, China*

**ARTICLE INFO**

Keywords:
Enhanced FFD
CFD method
PSO
SBD technique
Automatic optimization program

**ABSTRACT**

Hull optimization plays a crucial role in enhancing ship performance and efficiency. This study aimed to improve ship performance, particularly by reducing total resistance, through automated optimization methods. To this end, an integrated, fully automated optimization program was developed based on Python, incorporating Enhanced Free-Form Deformation (FFD) technology, scripted CFD numerical evaluation, and the Particle Swarm Optimization (PSO) algorithm. This program allowed precise control of hull form, improving efficiency while reducing costs. The KCS hull, known for its excellent resistance performance, was chosen as the optimization target, with the goal of minimizing total resistance by adjusting the bulbous bow line plan. The research results indicated that the optimized scheme exhibited lower resistance characteristics compared to the original design while satisfying design constraints. This study not only provides a new optimization strategy for ship design but also lays a foundation for future hull optimization research.

## 1. Introduction

Hull form optimization has always been an important research direction in the field of marine engineering. Hull form optimization can improve the economy, navigation stability, maneuverability, and safety of ships, while also reducing the impact on the environment. However, optimization strategies can vary. This study focuses on single-goal optimization, aiming to minimize the calm water resistance of the hull. Unlike holistic optimization, which addresses multiple factors simultaneously, single-goal optimization allows for more targeted and efficient improvement of specific ship performance aspects. The purpose of this study is to explore key technologies related to hull form optimization, including hull geometric reconstruction, resistance calculation methods, optimization algorithm application, and innovations in integrated technology.

With the development of the CFD method and the application of optimization technology, Li et al. [1] proposed a simulation-based Design (SBD) technology. Combining CFD and optimization algorithms, it has opened up a new era of data-driven, simulation-based hull optimization. This new approach allows designers to move away from traditional empirical or rule-based methods and instead leverage accurate simulations to

* Corresponding author.
E-mail address: bjzhang@shmtu.edu.cn

http://dx.doi.org/10.21278/brod75407
Received 17 May 2024; Received in revised form 15 September 2024; Accepted 30 September 2024
Available online 9 October 2024
ISSN 0007-215X; eISSN 1845-5859

explore complex design spaces. The integration of CFD and optimization algorithms enables more efficient performance predictions, reduces reliance on physical prototypes, and accelerates the design process, especially for complex or unconventional hull forms. The non-dominated sorting genetic algorithm II (NSGA-II) was used to optimize the design of a bulk carrier [2], demonstrating the applicability of the SBD framework for hull design. Choi et al. [3] used Sequential Quadratic Programming (SQP) and CFD to predict wave resistance and optimize hull forms. Zhang et al. [4] systematically elaborated the key technologies of hull design and optimization based on SBD technology. It includes numerical evaluation, hull geometry reconstruction, optimization method, comprehensive integration and other technologies. A complete technical system covering hull design and optimization was proposed. Zhang [5] employed the nonlinear programming (NLP) method, utilizing the Michell integral for wave resistance and the equivalent plate friction formula for friction resistance, optimizing a high-speed ship. The results indicate that SBD technology effectively advances hull design from traditional empirical approaches to more intelligent, knowledge-driven methods. Guo et al. [6] implemented the Lackenby and FFD deformation and reconstruction of the hull based on CAESES software. The commercial software STAR-CCM+ was used for numerical simulation, and the NSGA-II was used to optimize the design of the waterjet propulsion trimaran. The optimization results show that SBD technology can be used to solve complex hull design optimization problems. However, existing SBD frameworks often rely on external platforms like SHIPFLOW or CAESES, limiting flexibility and hindering full automation. To address this, this study proposes a fully automated, customizable framework integrating Enhanced FFD, automated CFD, and PSO optimization through Python, removing the need for external platforms and significantly enhancing flexibility, scalability, and automation.

Free-form deformation (FFD) is a commonly used method for deforming 3D objects, originally proposed by Sederberg and Parry [7], based on the earlier technique of Alan Barr [8]. It has seen rapid development, particularly in graphics and CAD. Miao et al. [9] used the FFD method to locally modify the KCS hull, achieving a significant reduction in total resistance. Li et al. [10] applied FFD for hull reconstruction and optimization, proving its feasibility. Zhao et al. [11] applied FFD to modify the bulbous bow of a fishing vessel using CAESES. However, traditional FFD faces limitations in deformation precision, especially for complex hull geometries, due to rigid control point configurations. This study proposes an Enhanced FFD technique, improving deformation accuracy with high-order B-spline models. Real-time interaction and adaptive sampling further optimize control points, enhancing flexibility in hull optimization.

Matulja et al. [12] developed a genetic algorithm-based hull optimization program. Zhang et al. [13] optimized Wigley hull using SHIPFLOW software, and Zhao et al. [11] used FFD with STAR-CCM+ and optimization algorithms for drag reduction in trawler hulls. Hamed [14] optimized trimaran hulls using HEEDS MDO software, and Hou et al [15] applied Kriging models for small underwater vehicle hulls. However, these frameworks often depend on predefined workflows, limiting flexibility and hindering full automation. In contrast, this study proposes a fully customizable approach integrating Enhanced FFD, automated CFD, and PSO optimization using Python, eliminating reliance on external platforms and enhancing adaptability to diverse hull forms while reducing design time.

This paper proposes a new hull form optimization model that integrates Enhanced FFD, optimization algorithms, and automated CFD evaluation into a fully automated SBD-based framework. The aim is to enhance the efficiency and flexibility of ship design, focusing on minimizing calm water resistance and improving design adaptability across different hull forms. This paper is organized as follows: Section 2 presents the key technologies used in the proposed optimization framework, including Enhanced FFD, the CFD-based evaluation methods and the optimization algorithm. Section 3 outlines the optimization algorithm and its integration with the hull form design process. Section 4 provides a detailed discussion of the results, comparing the optimized hull designs to the original. Finally, Section 5 concludes the paper by summarizing the findings and proposing future research directions.

## 2. The key technology of hull form optimization

### 2.1 Enhanced FFD

FFD is a commonly used 3D deformation technique that has been widely used in the field of hull optimization in recent years. It achieves deformation by creating a grid of control points around the object. Firstly, set up the control point grid and select key control points. Then, define the deformation direction and amplitude by moving the control points. The movement of control points will affect the shape of the object in the mesh and recalculate the vertex positions through the interpolation algorithm. Finally, the deformed model is generated. The deformation principle is shown in Fig. 1.

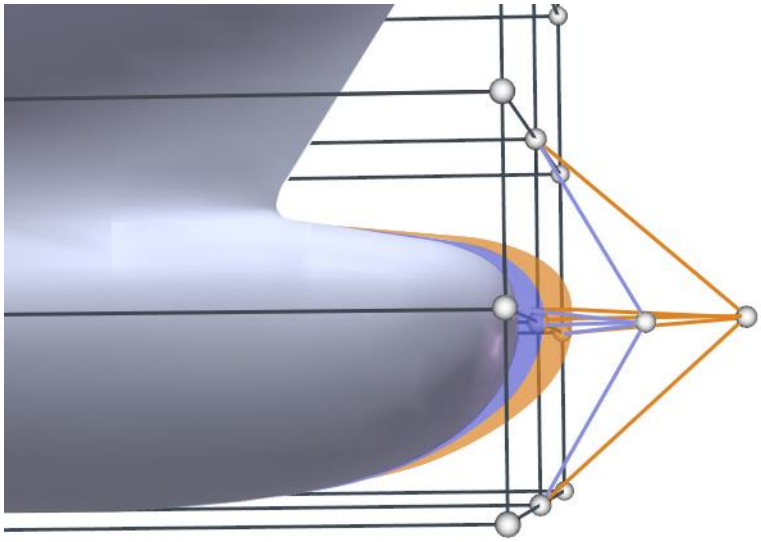

**Fig. 1** Deformation principle diagram

This paper implements an enhanced FFD algorithm based on Python programming. This algorithm is an extension of FFD, which provides greater flexibility and control capabilities. The enhanced FFD uses a high-order B-spline surface model to improve the accuracy of hull deformation. The number, location and layout of control points are optimized through interaction with the user interface and an effective sampling strategy, reducing the computational cost without affecting the accuracy. At the same time, volume constraints are introduced to ensure the rationality of the deformation results.

#### 2.1.1 B-spline surface model of high-degree

Previous FFD used in hull form optimization often used linear or polynomial interpolation to represent deformation. Enhanced FFD introduces a higher-order B-spline curve for parametric deformation. B-spline has the ability to describe the discontinuity of curves and surfaces [16]. It consists of B-spline basis functions. Let $B_{i,r}$ be a B-spline basis function. Its recursive definition [4] is as follows:

$$B_{i,r}(t)=\begin{cases}\begin{matrix}0 & t_i \le t \le t_{i+1}\\ 1 & otherwise\end{matrix}\Big\} & r=0\\ B_{i,r}(t)=\dfrac{t-t_i}{t_{i+r-1}-t_i}B_{i,r-1}(t)+\dfrac{t_{i+r}-t}{t_{i+r}-t_{i+1}}B_{i,r-1}(t) & r>0\end{cases} \tag{1}$$

where $i\in\{0,1,2,\cdots,q\}$, $q$ is the number of control points, $r$ is the order of the B-spline curve.

Enhanced FFD achieves the deformation effect by adjusting the positions of the control points. The deformed position $P'$ is calculated by interpolating the B-spline curves of all control points with the following formula:

$$P^{'}(u,v,w)=\sum_{i=0}^{q}\sum_{j=0}^{r}\sum_{k=0}^{s}B_{i,p}(u)B_{j,m}(v)B_{k,n}(w)P_{i,j,k}W_{i,j,k} \tag{2}$$

where $P_{i,j,k}$ is the position of the control points, $W_{i,j,k}$ is the weight function, $q,r,s$ are the numbers of control points on the surface, $p,m,n$ are the degrees of B-spline curves, and $u,v,w$ are the parameter coordinates before deformation.

B-spline surface has good mathematical properties such as local control, local support, and smoothness. It can accurately describe the local details and curvature changes of the surface, especially when the continuity and streamline of the hull need to be maintained. The enhanced FFD based on B-spline can provide more sophisticated global and local deformation effects, thereby improving accuracy and realism.

### 2.1.2 Effective sampling strategy

Traditional FFD technology usually uses a fixed number and layout of control points, which cannot be adjusted and customized according to specific needs. It is difficult to flexibly adapt to complex models. Enhanced FFD is highly customizable. The number, location and layout of control points can be dynamically adjusted through real-time interaction with the user interface. Researchers can flexibly select and adjust sampling strategies according to specific design requirements and goals. Including but not limited to uniform sampling, and hybrid sampling strategies combining uniform sampling with local dense sampling.

The uniform sampling method ensures a uniform distribution of control points throughout the design domain. It is suitable for scenarios that require overall control and deformation. The hybrid sampling strategy, which combines uniform sampling with local dense sampling, provides a solution for applications that require finer control in specific areas. This is because in the hull design, critical areas such as the bow or stern may require more detailed adjustments to optimize performance. As shown in the Fig. 2 taking the KCS hull as an example, the control points are set up by uniform sampling method for the whole ship, and the points are encrypted in the bow and stern areas.

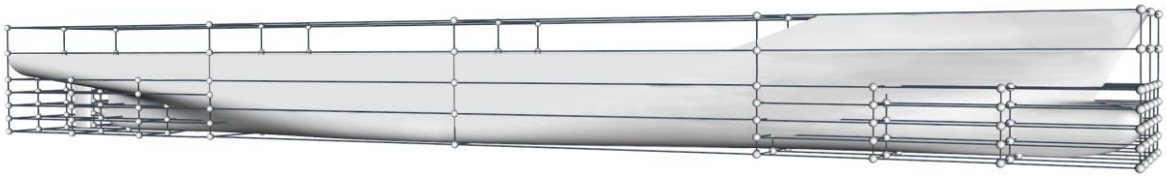

**Fig. 2** Mixed sampling strategy diagram

### 2.1.3 Volume constraint

In order to better meet the engineering needs of hull optimization. This paper introduces volume constraints in the Enhanced FFD. It can monitor the volume change during the deformation process to ensure that it does not exceed the preset error range. This can improve the rationality of the deformation results and the engineering feasibility. The volume calculation is also based on Python. Firstly, the area on the *XY* plane is calculated by the trapezoidal method, and then the volume can be obtained by integrating along the *Z* direction. Taking the hull displacement volume as an example, the calculation formula is as follows:

$$\nabla=\int_0^d A_W\,\mathrm{d}z=2\int_0^d\int_{-\frac{L}{2}}^{\frac{L}{2}}y\,\mathrm{d}x\mathrm{d}z \tag{3}$$

where $\nabla$ is the displacement volume of the hull at draught $\mathrm{d}$; $A_W$ is the area of the waterline at $z$ from the base plane. $y$ is the half-breadth of the waterline surface at $x$ on the $Oy$ axis; $L$ is the length of the water line, and the length between the vertical lines is generally taken in the calculation.

The Enhanced FFD module includes three steps: model parameterization, deformation and reconstruction. Volume calculation after deformation and before reconstruction can ensure the real-time effectiveness of volume constraints, thereby improving the stability of the optimization process and design

efficiency. It is also beneficial to maintain basic characteristics such as the hydrodynamic performance and structural strength of the hull.

In summary, Enhanced FFD has achieved a double improvement in computational efficiency and result rationality. The flexibility and applicability of this algorithm can make it an important tool for model deformation in multiple fields.

## 2.2 Numerical method

The CFD method has high accuracy and can comprehensively analyze the hull performance. Compared with actual model tests or sailing tests, the CFD method is less expensive. It is especially more economical and efficient for the comparison and optimization of multiple design schemes. Therefore, computational fluid dynamics (CFD) methods are used in this paper to perform numerical evaluation, and the tool selected is STAR-CCM+ [17].

Taking the KCS hull with excellent resistance performance as the design object. CFD method is used to calculate the total resistance of ships in calm water [18]. The main dimensions and specific simulation working conditions of the KCS hull are shown in Table 1, and the three-dimensional figure of the hull is shown in Fig. 3.

**Table 1** Main scale and simulation conditions

| Main scale | unit | KCS | working condition | unit | KCS |
|---|---|---|---|---|---|
| Scale ratio | - | 1:31.6 | Speed $V$ | (m/s) | 2.196 |
| Length at waterline $L_{WL}$ | (m) | 7.3570 | Trim | (m) | 0 |
| Breadth $B$ | (m) | 1.019 | Froude Number $Fr$ | - | 0.26 |
| Draft $d$ | (m) | 0.3418 | Reynolds Number $Re$ | - | $1.418\times10^{7}$ |
| Wetted surface area $S$ | ($m^2$) | 9.5527 | Density $\rho$ | ($kg/m^3$) | 997.561 |
| Displacement volume | ($m^3$) | 1.6490 | $L/B$ | - | 7.2198 |
| $\nabla/L^3$ | - | $4.14\times10^{-3}$ | $B/d$ | - | 2.981 |

**Fig. 3** Hull three-dimensional diagram

The CFD numerical evaluation is based on Python directly calling STAR-CCM+. In order to ensure the automatic optimization, macro recording is used in this paper to implement the steps of model replacement, meshing, resistance setting and result export. Therefore, the consistency of numerical calculation methods for different hull schemes is also guaranteed.

The specific settings are as follows [19]: the fluid is assumed to be two-phase, consisting of air and water, with both phases considered viscous and incompressible. The fluid motion is governed by the Navier-Stokes equations and the continuity equation, ensuring mass conservation and accurately describing the dynamics of incompressible viscous fluids. For the two-phase flow model, the interface between air and water is tracked using a volume fraction conservation equation, allowing accurate simulation of phase interactions and surface wave formation. The K-Epsilon model is used to describe the dynamic behavior and energy dissipation of turbulence. The VOF method is employed to track the free surface between phases, with the momentum equation and volume fraction governing the two-phase flow. The finite volume method is used to discretize the control equations, applying a central difference scheme for the diffusion term and a second-order upwind scheme for the convection term, which reduces numerical dissipation and improves simulation

accuracy. According to the recommendations of ITTC [20], the computational domain and boundary conditions are set in this paper, as shown in Fig. 4. Wave damping is attached to the rest of the computational domain boundaries, except for the top and bottom boundaries of the computational domain, to avoid the influence of wave reflection on the flow field around the hull.

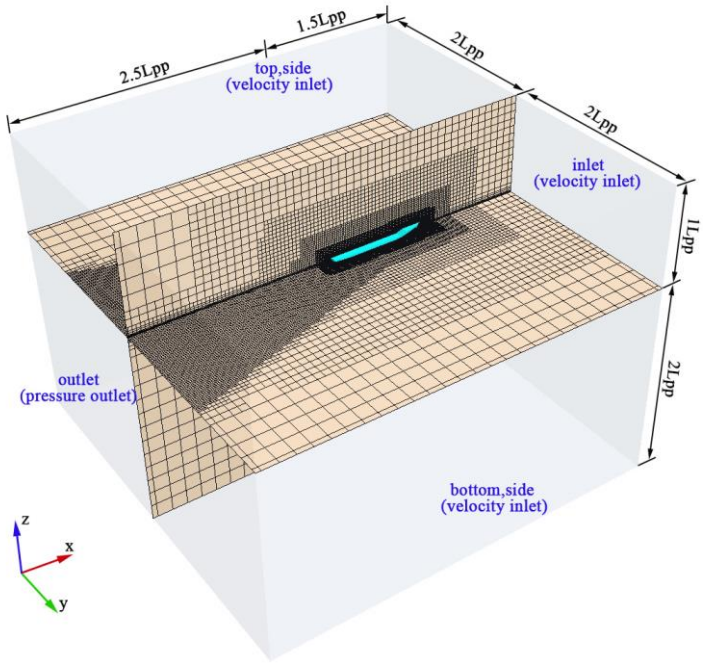


**Fig. 4** Computational domain and boundary conditions

In addition, the size of the equal-scale grid foundation is 0.15 m, and the total number of grids is 1.78 million. The hull grid and free surface grid are shown in Fig. 5. This paper adopts the method of local encryption of the bow to better capture the resistance changes caused by the deformation of the bulbous bow.

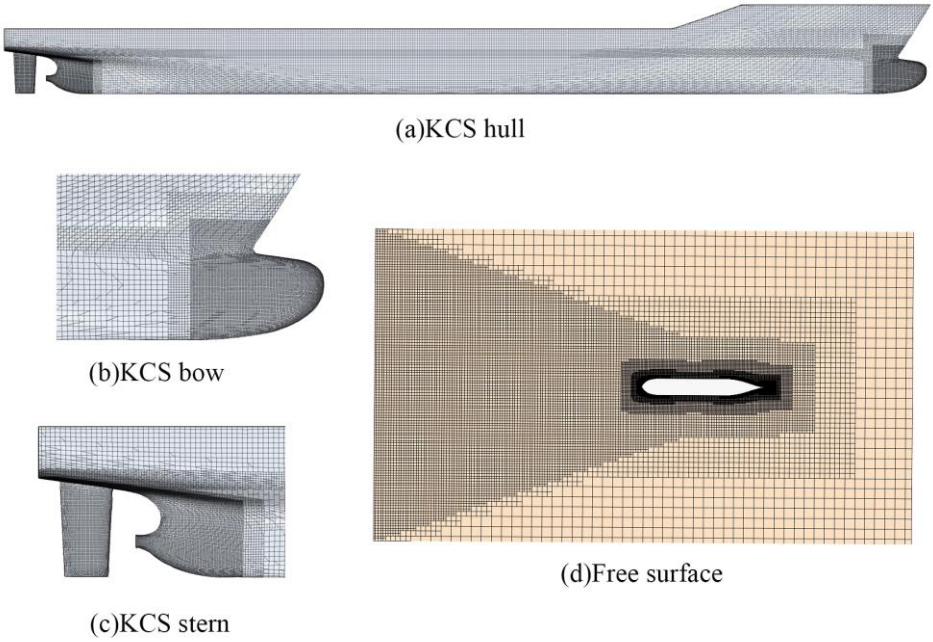


**Fig. 5** Hull grid and free surface grid

### 2.2.1 Uncertainty analysis

In CFD calculations, mesh generation has a significant impact on both the accuracy of the results and the computational speed. The precision of the mesh is crucial for predicting accurate outcomes. Therefore,

before conducting optimization design evaluations, it is necessary to perform a mesh uncertainty analysis based on experimental model data. According to the ITTC recommendations, a uniform refinement ratio is applied, with the base grid size ratios for the three mesh groups set to $r_i = \sqrt{2} \approx 1.414$. In this paper, three sets of grid settings are set up. The main difference lies in the basic size of the grid. According to the grid density, the results of the three examples can be divided into $S_1$ (fine), $S_2$ (medium), $S_3$ (coarse), as shown in Fig. 6.

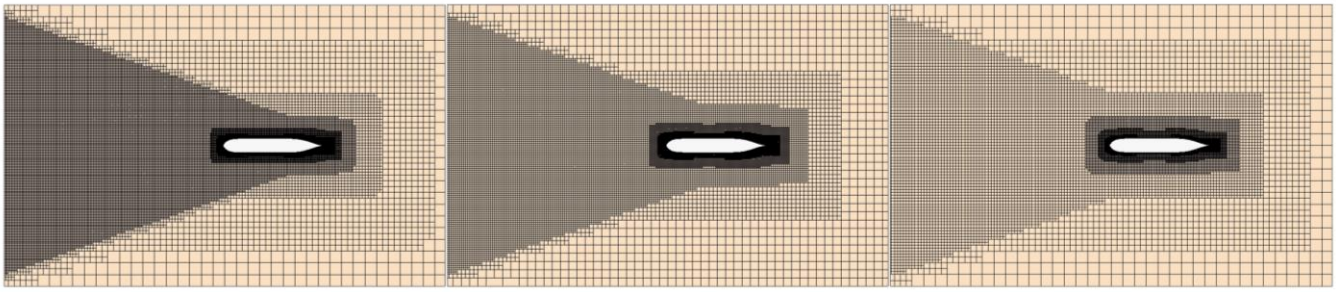


**Fig. 6** Three sets of grids for KCS hull

The uncertainty is calculated as follows:

$$\varepsilon_{i,21} = S_{i,medium} - S_{i,fine} = S_2 - S_1 \tag{4}$$

$$\varepsilon_{i,32} = S_{i,coarse} - S_{i,medium} = S_3 - S_2 \tag{5}$$

$$R_i = \frac{\varepsilon_{i,21}}{\varepsilon_{i,32}} \tag{6}$$

where $S_1$ (fine), $S_2$ (medium) and $S_3$ (coarse) correspond to solutions with fine, medium and coarse input parameters respectively. $\varepsilon_{i,21}$ represent the deviation terms between $S_1$ grid and $S_2$ grid, and $\varepsilon_{i,32}$ represent the deviation terms between $S_2$ grid and $S_3$ grid.

$R_i$ can get three convergence conditions: (1) $0 < R_i < 1$: monotone convergence; (2) $R_i < 0$: oscillatory convergence; (3) $R_i > 1$: divergence.

For $0 < R_i < 1$, the error $\delta^*_{RE_{i,1}}$ of the three solutions is usually determined using generalized Richardson extrapolation, and an estimate of the error and the order of Precision $p_i$ can be obtained:

$$\delta^{*(1)}_{RE_{i,1}} = \frac{\varepsilon_{i,21}}{r_i^{p_i} - 1} \tag{7}$$

$$p_i = \frac{ln(\varepsilon_{i,32} / \varepsilon_{i,21})}{ln(r_i)} \tag{8}$$

$$\delta^*_{i,1} = C_i \delta^*_{RE_{i,1}} = C_i \frac{\varepsilon_{i,21}}{r_i^{p_i} - 1} \tag{9}$$

$$C_i = \frac{r_i^{p_i} - 1}{r_i^{p_{iest}} - 1} \tag{10}$$

where $C_i$ is the correction coefficient, $p_{iest}$ is the estimate of the first precision limit order. Since the spacing size is 0 and reaches the asymptotic range, such that $C_i \to 1$, $p_{iest} = 2$.

When $C_i$ is much less than or greater than 1:

$$U_i = (|C_i| + |1 - C_i|)\left|\delta^*_{RE_{i,1}}\right|, \quad |1 - C_i| > 0.125 \tag{11}$$

$$E = D - S_1 \tag{12}$$

$$U_V \approx \sqrt{U_D^2 + U_i^2} \tag{13}$$

where $U_D = 2.5\%D$, $D$ is the experimental value, and $E$ is the difference between $D$ and $S_1$.

In 2002, Wilson and Stern further revised the formulas of $U_i$ and $U_V$ on the basis of the above formula. The uncertainty $U_{i_C}$ and the verification uncertainty $U_{V_C}$ after revision can be calculated as:

$$S_C = S_1 - \delta^*_{i,1} \tag{14}$$

$$E_C = D - S_C \tag{15}$$

$$U_{i_C} = |1 - C_i|\left|\delta^*_{RE_{i,1}}\right|, \quad |1 - C_i| > 0.25 \tag{16}$$

$$U_{V_C} \approx \sqrt{U_D^2 + U_{i_C}^2} \tag{17}$$

In this paper, an uncertainty analysis was conducted on the total resistance coefficient of the KCS model, and the calculation results are shown in Table 2, 3 and 4. From the table, $|E| < U_V$ and $|E_C| < U_{VC}$, that is, the current calculation results are valid and meet the requirements.

**Table 2** Total resistance coefficient of three sets of grids

| | Coarse $S_3$ | Medium $S_2$ | Fine $S_1$ | $D$ |
|---|---|---|---|---|
| Mesh number | 1018301 | 1779582 | 3338975 | - |
| $C_t$ ($10^{-3}$) | 3.562 | 3.624 | 3.661 | 3.711 |

**Table 3** Verification of total resistance coefficient calculation value

| | $r_i$ | $R_i$ | $p_i$ | $\delta^*_{RE_{i,1}}(\%D)$ |
|---|---|---|---|---|
| Results | 1.414 | 0.598 | 1.485 | -1.493 |

**Table 4** Validation of total resistance coefficient calculation value

| Error | Results ($10^{-4}$) | Uncertainty | Results ($10^{-4}$) | Relationship |
|---|---|---|---|---|
| $E$ | 0.497 | $U_V$ | 0.926 | $\|E\| < U_V$ |
| $E_C$ | 0.125 | $U_{V_C}$ | 0.764 | $\|E_C\| < U_{VC}$ |

The medium grid is finally selected as the basis for calculations. The reason is that the medium grid setting can not only ensure a certain accuracy, but also improve the calculation speed and save computing resources. Therefore, the final mesh setting adopted is set according to that of $S_2$.

### 2.2.2 Verification of the Numerical Method

In order to further verify the feasibility and accuracy of the above numerical method, the total resistance of the KCS model at different speeds was simulated based on the selected medium grid settings. The

numerical results were then compared with experimental data from the literature [21]. The conversion method from the model to the actual ship resistance is consistent with the literature. The conversion method is as follows:

$$C_{\mathrm{t}} = \frac{R_{\mathrm{t}}}{0.5\rho V^2 S} \tag{18}$$

where, $C_t$ is the total resistance coefficient, $R_t$ is the total resistance, $\rho$ is the density of water, $V$ is the speed of the ship model, and $S$ is the wet surface area of the ship model.

The error between the numerical calculation value and the experimental value of the KCS hull is shown in Table 5.

**Table 5** Comparison of numerical results

| $Fr$ | $C_t$_Exp ($10^{-3}$) | $C_t$ _ CFD ($10^{-3}$) | Error (%) |
|---|---|---|---|
| 0.19 | 3.475 | 3.409 | 1.89% |
| 0.22 | 3.467 | 3.398 | 1.99% |
| 0.26 | 3.711 | 3.624 | 2.34% |
| 0.28 | 4.501 | 4.374 | 2.82% |

It can be seen that the error is kept within 3%. This shows that the CFD settings in this paper have a certain degree of accuracy and can meet the actual needs of the project. At the same time, it can also serve as a basis for supporting the reliability of the optimization results.

## 2.3 Optimal algorithm

Hull form optimization is a complex engineering challenge, and choosing the appropriate optimization algorithm can greatly enhance efficiency. In this paper, the classical particle swarm optimization algorithm is used to solve the optimization problem [22]. It has good results in fast convergence and avoids falling into local optimal solutions earlier.

PSO is an optimization algorithm inspired by swarm intelligence, mimicking the foraging behavior of bird flocks to find an optimal solution. Each particle in the swarm represents a candidate solution, which updates its position based on both its own best-known position ($P_{\mathrm{best}}$) and the global best-known position ($G_{\mathrm{best}}$). The position update is governed by the following equations:

$$V_i(\mathrm{t}+1) = \omega V_i(\mathrm{t}) + c_1 r_1 (P_{best}(i) - X_i(t)) + c_2 r_2 (G_{best} - X_i(t)) \tag{19}$$

$$X_i(t+1) = X_i(t) + V_i(\mathrm{t}+1) \tag{20}$$

where, $V_i(\mathrm{t})$ is the velocity of the particle, $X_i(t)$ is the position of the particle, $P_{\mathrm{best}}$ is the individual best position of the particle, $G_{\mathrm{best}}$ is the global best position, $\omega$ is the inertia weight, $c_1$ and $c_2$ is the learning factors, $r_1$ and $r_2$ are random numbers between 0 and 1.

The iterative process of PSO is as follows:

(1) Velocity Update: The velocity of each particle is updated according to its current velocity, the distance to its best-known position, and the distance to the global best-known position.

(2) Position Update: The new position of the particle is calculated based on the updated velocity.

(3) Boundary Handling: After updating the position, boundary checks are performed to ensure the particle remains within the feasible solution space, avoiding unrealistic or invalid solutions.

(4) Fitness Evaluation: Each particle's new position is evaluated using CFD to determine the total resistance value of the hull, which serves as the fitness function.

(5) $P_{best}$ and $G_{best}$ Update: If the new position yields a better fitness value than the previous best-known position, the particle's best-known position is updated. The global best-known position is updated if any particle achieves a better fitness than the current global best.

(6) Termination Condition: The algorithm checks if the termination condition is met (e.g., maximum iterations or satisfactory fitness level). If met, the optimization ends; otherwise, the process repeats.

This process is depicted in Fig. 7, illustrating how the PSO algorithm, integrated with Enhanced FFD and CFD, iteratively optimizes the hull form. The hull parameters define the dimensions of the particles, and each iteration refines the hull shape through these systematic updates and evaluations.

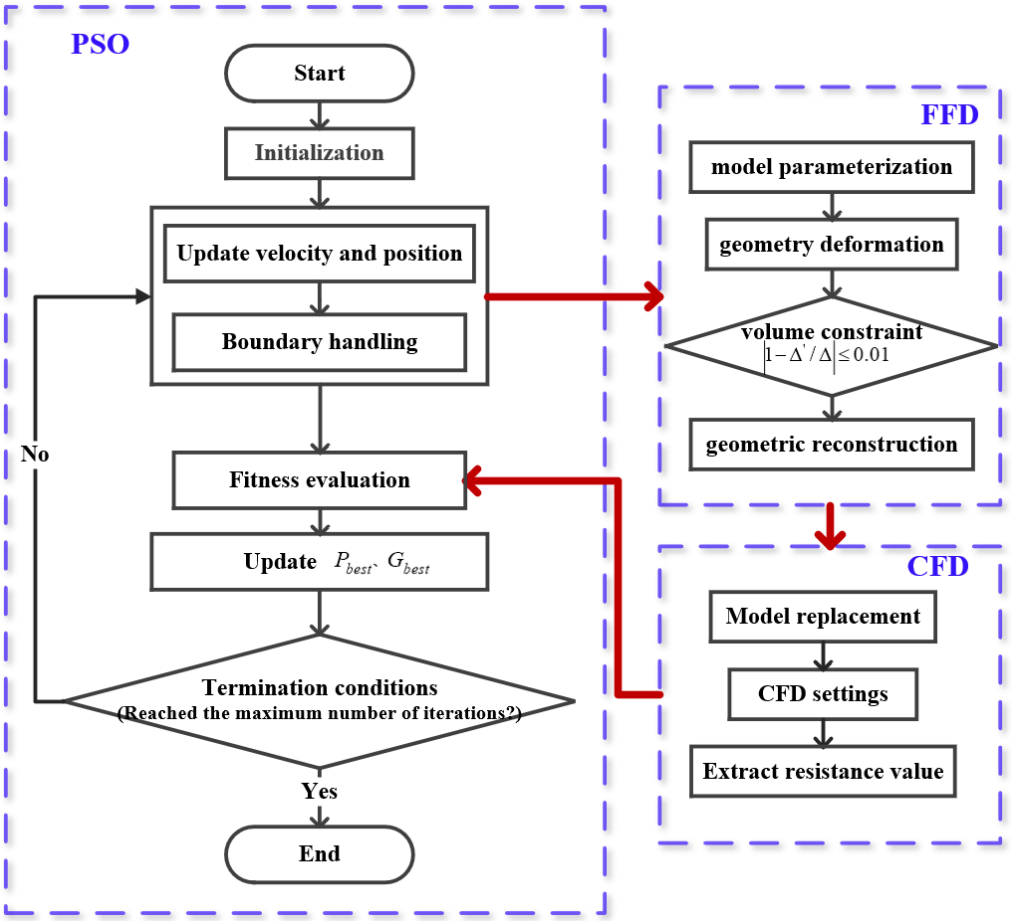


**Fig. 7** Hull form optimization flow chart

In order to verify the effectiveness of the PSO program in this paper, the Rosenbrock function and the Rastrigin function are used to test its convergence. Rosenbrock function is a classical non-convex optimization problem, which is suitable for evaluating the performance of optimization algorithms. The expression is as follows:

$$f(x)=\sum_{i=1}^{n-1}[100(x_{(i+1)}-x_i^2)^2+(1-x_i)^2] \tag{21}$$

The Rastrigin function can often be used to test the ability of the algorithm to avoid falling into a local minimum. Its expression is as follows:

$$f(x)=\sum_{i=1}^{D}[x_i^2-10\cos(2\pi x_i)+10] \tag{22}$$

The maximum number of iterations is set to 1000, the space dimension is 10, and the convergence curve is shown in Fig. 8. The convergence curve shows a gradual convergence trend, indicating that the PSO program based on Python programming can converge quickly and avoid falling into local optimal solution.

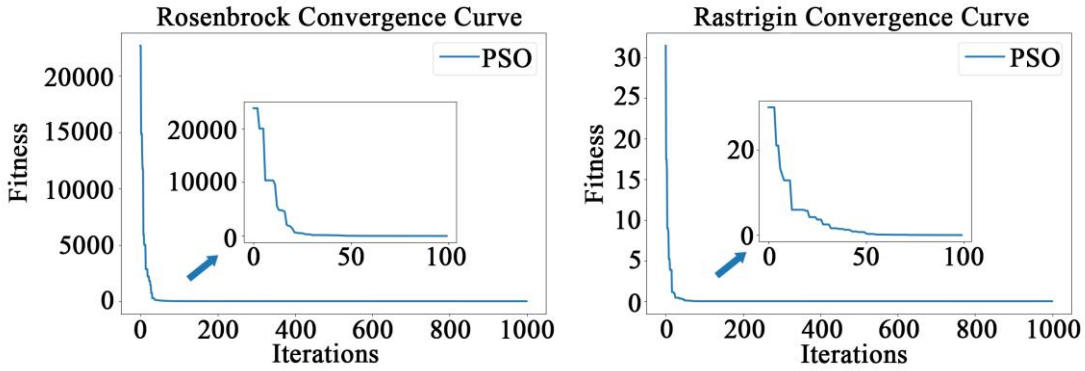


**Fig. 8** PSO convergence curve

## 2.4 Comprehensive integration

The entire process of hull optimization is carried out automatically without human intervention. How to integrate the many key technical modules involved is a problem that must be solved to achieve automatic optimization. This paper implements Enhanced FFD, CFD numerical simulation and optimization algorithms based on programming and scripting. A fully automatic optimization framework based on SBD is constructed. The above technologies are integrated based on Python and script calls to obtain an automatic hull optimization program. The program has high flexibility and customizability. It can better adapt to specific hull optimization problems and can be expanded and modified as needed. The principle of automatic optimization framework is shown in Fig. 9.

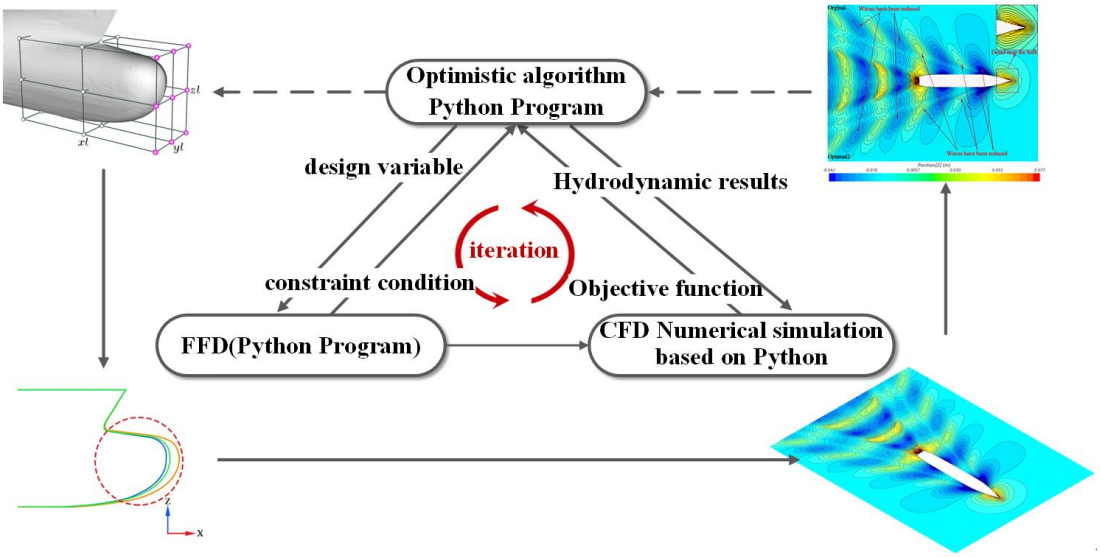


**Fig. 9** Principle of hull form optimization

Comprehensive integration does not only refer to the simple integration of various modules, but also ensures that the data between modules can be effectively exchanged and circulated. The details of data transmission in the comprehensive integration of this paper are shown in Fig. 10.

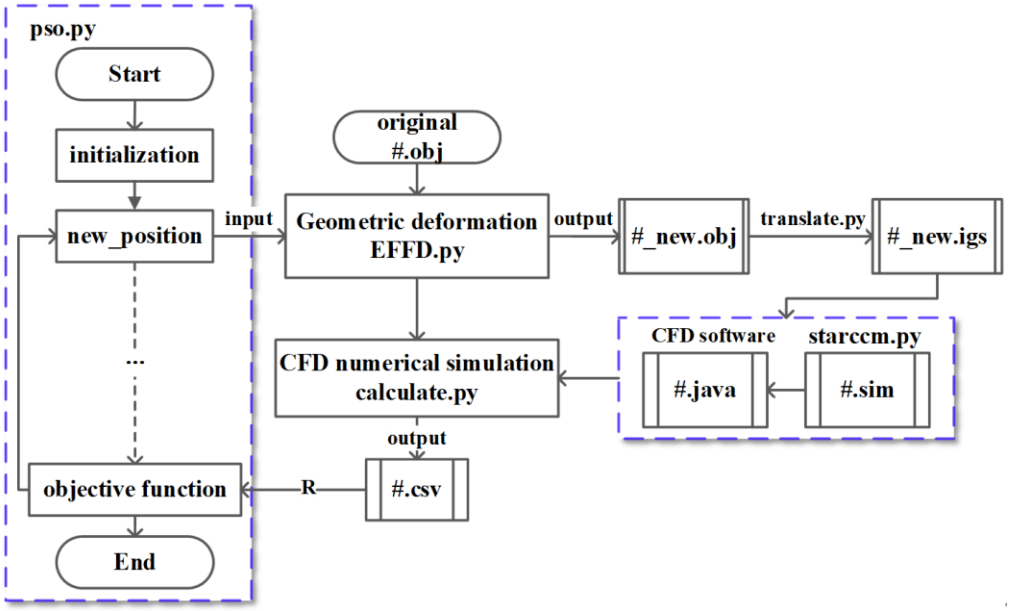


**Fig. 10** Data transfer diagram

This paper independently constructs a hull optimization process with high flexibility and customization, which can better adapt to optimization problems under different conditions.

## 3. Mathematical model for Optimal Design of Bulbous Bow

In this paper, the KCS hull with excellent resistance performance is taken as the design object, and the line type of its bulbous bow is optimized. The main dimensions and simulation conditions are listed in Table 1. The bulbous bow can directly affect the streamline and resistance performance of the hull. By locally deforming the bulbous bow with Enhanced FFD, a significant drag reduction effect can be achieved in a relatively short period of time, thereby quickly improving the performance of the hull.

### 3.1 Objective function

This optimization work aims to obtain the hull with the minimum total resistance, so the optimization goal is to minimize the total resistance $R_t$. The objective function expression is:

$$F = \min(R_t) \tag{23}$$

Total resistance is one of the important indicators to measure the performance of a ship. Reducing total resistance can improve the ship's operating efficiency, reduce energy consumption, and thus reduce navigation costs. In addition, minimizing total resistance is an important goal of design and optimization in many engineering practices. Therefore, minimizing total resistance is in line with engineering practice.

### 3.2 Design variables and constraints

Considering the computational cost and optimization efficiency, this optimization work focuses on the bulbous bow area. That is, only the bulbous bow area is intercepted for optimization, and a uniform sampling strategy is adopted in this area. The bulbous bow is a key part of hull form optimization, and it directly affects the resistance performance of the ship. By evenly distributing control points in the bulbous bow area, the accuracy of deformation and the effectiveness of optimization are ensured. The deformation area after the box selection is also called the control body, and the length of the control body in the $x, y, z$ direction is set to $xl, yl, zl$, as shown in Fig. 11.

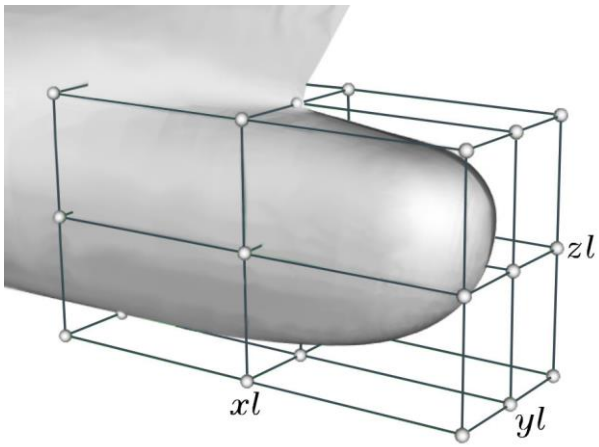


**Fig. 11** Control body

In the figure, there are 27 control points surrounding the bulbous bow to control its deformation. On the one hand, increasing the number of control points can provide greater flexibility and precision. On the other hand, if there are too many control points, it will increase the complexity of calculation and memory usage, making the operation difficult. It may even make the deformation result of the surface worse than expected.

The following aspects are mainly considered for setting design variables. First, considering the high computational time cost of CFD itself, multivariable optimization usually requires more computing resources and time. Second, although a single variable may limit the optimization potential, it is easier to achieve good results if the design variables with greater impact on resistance can be selected based on prior knowledge and experience. Finally, single variable optimization is a step-by-step optimization process, which can gradually improve the design and gradually improve the hull performance while simplifying the problem and focusing on the key points.

Therefore, this paper only selects a set of control points as independent variables for the optimization design, and their definitions are shown in Table 6. The displacement parameterization of the control points is controlled by $xl$ . By adjusting $xl$ , the position of the purple control points in the schematic diagram can be effectively changed, thereby modifying the geometric form of the bulbous bow while keeping the rest of the hull basically unchanged. In addition, the out-of-bounds processing ensures that the design variable value remains within the definition domain. The displacement constraint is $\left|(\Delta^{'}-\Delta)/\Delta\right| \le 0.01$ , and the ship breadth and draft remain unchanged.

**Table 6** Definition of design variable

| schematic diagram | variable | range of variation (mm) |
|---|---|---|
| 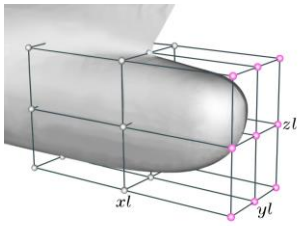 | *xl* | ±200 |

## 3.3 Optimal results

The computational simulations were performed using two Intel 18-core 3.6 GHz workstations. For each newly generated hull design, a full CFD simulation was conducted, with each simulation taking approximately 6-7 hours. Over the course of the optimization process, a total of 100 design iterations were evaluated. Due to boundary violations and other constraints, some results were excluded from further analysis.

In this paper, two representative optimization results were selected from multiple design schemes. The total resistance distribution of different schemes during the optimization process is shown in Fig. 12.

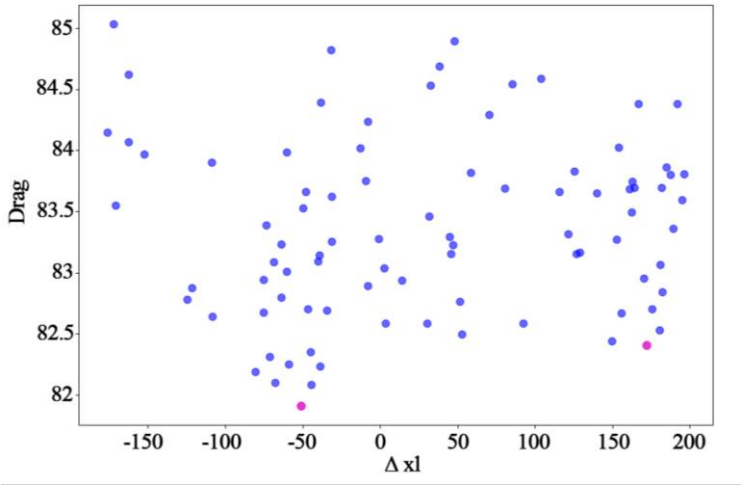


**Fig. 12** Scatter plot of optimization results

The optimization results of the two schemes are summarized in Table 7 and Fig. 13, showing the comparison between the original design and the optimized hull forms in terms of drag coefficients and bulbous bow shapes.

**Table 7** Comparison between Design and Optimal

| Optimal Cases | Total drag coefficient $C_t(10^{-3})$ | | | Residual drag coefficient $C_r(10^{-3})$ | | |
|---|---|---|---|---|---|---|
| | Design | Optimized | % | Design | Optimized | % |
| Optimal Case1 | 3.624 | 3.567 | 1.53% | 0.8289 | 0.7891 | 4.81% |
| Optimal Case2 | 3.624 | 3.586 | 1.04% | 0.8289 | 0.7911 | 4.57% |

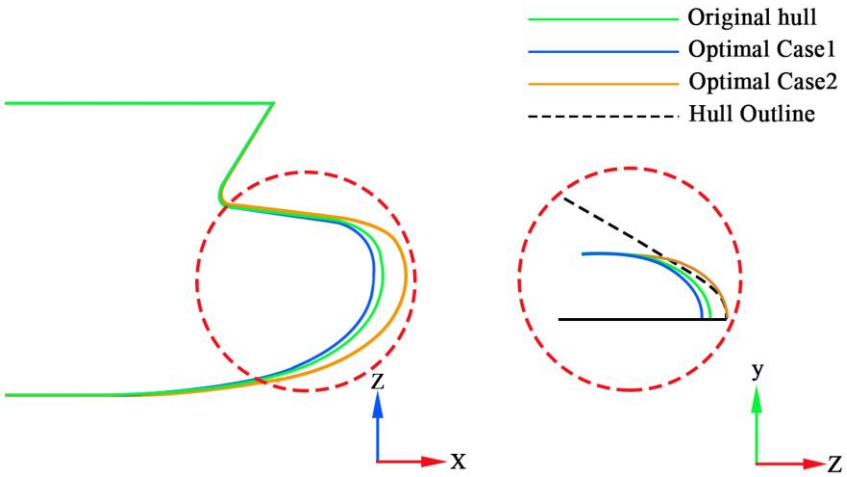


**Fig. 13** Comparison of bulbous bow

As seen in Table 7, Optimal Case 1 reduces the total drag coefficient by 1.53%, while Optimal Case 2 achieves a reduction of 1.04%. Both cases significantly lower the residual drag coefficient, with Optimal Case 1 achieving a 4.81% reduction and Optimal Case 2 showing a 4.57% reduction. These improvements in drag reduction directly translate into enhanced hydrodynamic performance and improved fuel efficiency. In Fig. 13, the comparison of the bulbous bow shapes reveals that Optimal Case 1 results in a slightly reduced displacement volume, whereas Optimal Case 2 increases the displacement. These variations in displacement

affect the hull's buoyancy, stability, and carrying capacity. While Optimal Case 1 offers a more efficient reduction in drag, making it suitable for applications where fuel economy and sailing efficiency are prioritized, Optimal Case 2 provides enhanced stability and load-carrying potential, which may be advantageous in scenarios requiring greater displacement.

In addition, Fig. 14 shows the comparison of the free surface wave amplitude cloud diagrams for the original design and the two optimized schemes. The figure reveals significant differences in wave amplitude distribution between the original scheme (labeled "Original") and the optimized schemes (labeled "Optimal Case 1" and "Optimal Case 2"). The original scheme exhibits relatively high wave amplitudes, particularly near the bulbous bow, where the wave crest height is notably elevated, and the wave pattern is more widespread. These features contribute to increased wave resistance, adversely affecting the hull's hydrodynamic performance. In contrast, the optimized schemes show substantial improvements: wave amplitudes are significantly reduced, especially in the bulbous bow area, where the wave crest height is lowered, and the wave pattern becomes more concentrated and smooth. This demonstrates the effectiveness of the optimization in reducing wave resistance and improving hydrodynamic performance.

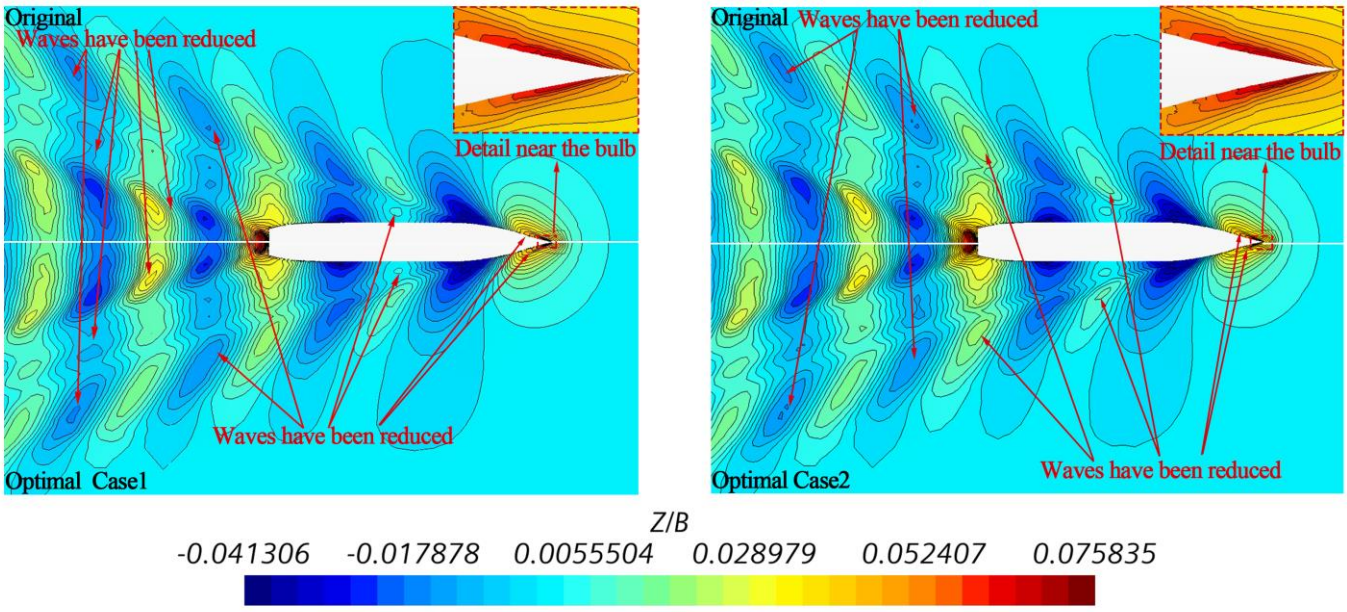


**Fig. 14** Comparison of wave amplitude cloud diagrams

Fig. 15 complements this analysis by comparing the water surface elevation between the original and optimized hull designs. It presents wave profiles at two longitudinal cross-sections of the free surface: $y = 0$ and $y = 0.55$. This comparison not only visually confirms the reduction in wave amplitude near the bulbous bow but also quantitatively validates these improvements through calculated differences in water surface elevation. Together, these figures provide a comprehensive view of the optimization's impact on wave amplitude and hydrodynamic performance.

In conclusion, the optimization results demonstrate significant improvements in hull performance, with Optimal Case 1 excelling in reducing drag and enhancing sailing efficiency, while Optimal Case 2 offers advantages in terms of stability and load capacity. The effectiveness of the optimization strategy based on enhanced FFD and CFD methods was verified by comparative analysis before and after optimization. These findings provide valuable insights and a solid reference for future hull design and optimization. Further research can explore more diverse optimization methods and design variables to achieve even greater performance and efficiency enhancements.

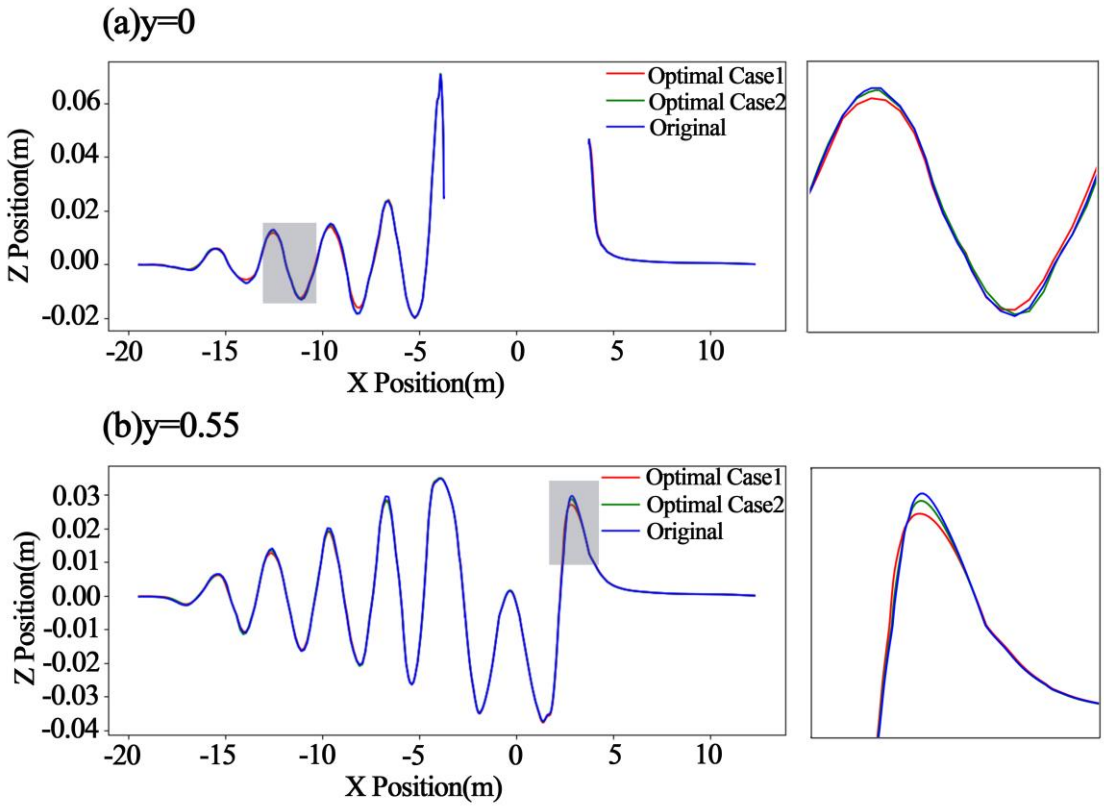


**Fig. 15** Comparison of Water Surface Elevation

## 4. Conclusion

This paper presents a fully automated hull optimization program based on Simulation-Based Design (SBD), integrating Enhanced FFD, automated CFD evaluation, and Particle Swarm Optimization (PSO). The main conclusions drawn from the optimization of the KCS hull are as follows:

(1) The Enhanced FFD technique effectively characterizes complex local hull geometries, allowing for precise deformations even in challenging areas. Coupled with automated CFD evaluation, this significantly enhances the efficiency and consistency of the optimization process. The modular design of the proposed optimization framework provides high scalability and compatibility, enabling easy integration of future technological advancements and supporting ongoing innovation in the shipping industry.

(2) The optimization framework shows great potential in practical ship design applications. By automating the design process, it reduces both the design cycle and associated costs. Additionally, optimizing the hull form leads to energy conservation and emission reduction, laying the groundwork for future research on smart ships and autonomous navigation.

(3) Despite these advancements, the proposed framework has several limitations. First, the Enhanced FFD technique may encounter challenges when applied to highly complex or unconventional hull geometries, where fine control of deformation remains a constraint. Second, the current framework is designed for single-goal optimization, focusing on minimizing calm water resistance. Future work could explore multi-objective optimization to balance resistance, stability, and seakeeping performance. Additionally, while the automated CFD evaluation improves process efficiency, high-resolution simulations still require significant computational resources. Lastly, the framework is currently validated primarily for KCS hull, and further studies are needed to extend its applicability to other vessel types, such as catamarans or high-speed crafts.

(4) To reduce the computational cost of high-fidelity CFD simulations, future research should explore surrogate modeling techniques, such as radial basis function neural networks, and parallel computing to improve efficiency. Additionally, expanding the framework to support multi-objective optimization could enhance ship design by optimizing multiple design aspects simultaneously. Further studies are also needed to

validate the framework's applicability across various vessel types, including high-speed vessels and bulk carriers, to ensure its robustness and versatility.

## REFERENCES


[1] Li, S. Z., Zhao, F., Ni, Q. J., 2013. Multiobjective optimization for ship hull form design using SBD technique. *Computer Modeling in Engineering & Sciences*, 92(2), 123-149. https://doi.org/10.3970/cmes.2013.092.123

[2] Li, S. Z., Zhao, F., Ni, Q. J., 2014. Bow and stern shape integrated optimization for a full ship by a simulation-based design technique. *Journal of Ship Research*, 58(02), 83-96. https://doi.org/10.5957/JOSR.58.2.130008

[3] Choi, H. J., Yoon, H. S., 2016. Research on hull-form optimization of a passenger ship using hull-form modification algorithm with Gaussian distribution function. *Brodogradnja*, 67(3), 1-15. https://doi.org/10.21278/brod67301

[4] Zhang, B. J., Zhang, S. L., 2019. Research on ship design and optimization based on simulation-based design (SBD) technique. *Springer*, Singapore. https://doi.org/10.1007/978-981-10-8423-2

[5] Zhang, B., 2020. Research on ship hull optimisation of high-speed ship based on viscous flow/potential flow theory. *Polish Maritime Research*, 27 (1), 18-28. https://doi.org/10.2478/pomr-2020-0002

[6] Guo, J., Zhang, Y., Chen, Z., Feng, Y., 2020. CFD-based multi-objective optimization of a waterjet-propelled trimaran. *Ocean Engineering*, 195(1), 106755. https://doi.org/10.1016/j.oceaneng.2019.106755

[7] Sederberg, T. W., Parry, S. R., 1986. Free-form deformation of solid geometric models. *Computer Graphics*, 20(4), 151-160. https://doi.org/10.1145/15886.15903

[8] Barr, A. H., 1984. Global and local deformations of solid primitives. *Computer & Graphics*, 18(3), 21-30. https://doi.org/10.1145/964965.808573

[9] Miao, A., Wan, D., 2020. Hull Form Optimization Based on an NM+CFD Integrated Method for KCS. *International Journal of Computational Methods*, 17(10), 2050008. https://doi.org/10.1142/S0219876220500085

[10] Li, S., Zhu, F., Hou, X., Ni, Q., 2022. Application of mesh deformation and adaptive method in hullform design optimization. *Journal of Marine Science and Technology*, 27(6), 1-10. https://doi.org/10.1007/s00773-021-00851-9

[11] Zhao, C., Wang, W., Jia, P., Xie, Y., 2021. Optimisation of hull form of ocean-going trawler. *Brodogradnja*, 72(4), 33-46. https://doi.org/10.21278/brod72403

[12] Matulja, D., Dejhalla, R., 2013. Optimization of the ship hull hydrodynamic characteristics in calm water. *Brodogradnja*, 64(4), 426-436.

[13] Zhang, S., Tezdogan, T., Zhang, B., Lin, L., 2021. Research on the hull form optimization using the surrogate models. *Engineering Applications of Computational Fluid Mechanics*, 15(1), 747-761. https://doi.org/10.1080/19942060.2021.1915875

[14] Hamed, A., 2022. Multi-objective optimization method of trimaran hull form for resistance reduction and propeller intake flow improvement. *Ocean Engineering*, 244(3), 110352. https://doi.org/10.1016/j.oceaneng.2021.110352

[15] Hou, S., Zhang, Z., Lian, H., Xing, X., Gong, H., Xu, X., 2022. Hull shape optimization of small underwater vehicle based on Kriging-based response surface method and multi-objective optimization algorithm. *Brodogradnja*, 73(3), 111-134. https://doi.org/10.21278/brod73307

[16] Ban, D., Blagojević, B., Čalić, B., 2014. Analytical solution of global 2D description of ship geometry with discontinuities using composition of polynomial radial basis functions. *Brodogradnja*, 65(2), 1-22.

[17] Martić, I., Degiuli, N., Borčić, K., Grlj, C. G., 2023. Numerical Assessment of the Resistance of a Solar Catamaran in Shallow Water. *Journal of marine science and engineering*, 11(9), 1706. https://doi.org/10.3390/jmse11091706

[18] Ma, Z., Ji, N., Zeng, Q., Deng, X., Shi, C., 2024. Influence of scale effect on flow field offset for ships in confined waters. *Brodogradnja*, 75(1), 1-22. https://doi.org/10.21278/brod75106

[19] Hadi, E. S., Tuswan, T., Azizah, G., Ali, B., Samuel, S., Hakim, M. L., Satrio, D., 2023. Influence of the canal width and depth on the resistance of 750 DWT Perintis ship using CFD simulation. *Brodogradnja*, 74(1), 117-144. https://doi.org/10.21278/brod74107

[20] ITTC. 2014. ITTC – Recommended Procedures and Guidelines - Practical Guidelines for Ship CFD Applications, *ITTC – Recommended Procedures and Guidelines*. https://www.ittc.info/media/9773/75-03-02-03.pdf.

[21] Lungu, A., 2019. Numerical Simulation of the Resistance and Self-Propulsion Model Tests. *Journal of Offshore Mechanics and Arctic Engineering*, 142(2), 1-37. https://doi.org/10.1115/1.4045332

[22] Shami, T. M., El-Saleh, A. A., Alswaitti, M., Al-Tashi, Q., Summakieh, M. A., Mirjalili, S., 2022. Particle swarm optimization: A comprehensive survey. *IEEE Access*, 10, 10031-10061. https://doi.org/10.1109/ACCESS.2022.3142859